



# Application of deep learning and spectral deconvolution for estimating mineral abundances of zeolite, Mg-sulfate and montmorillonite mixtures and its implications for Mars



Gayantha R.L. Kodikara <sup>a,\*</sup>, Lindsay J. McHenry <sup>a</sup>, Freek D. van der Meer <sup>b</sup>

<sup>a</sup> Department of Geosciences, University of Wisconsin-Milwaukee, 3209 N, Maryland Ave, Milwaukee, WI, 53211, USA

<sup>b</sup> University of Twente, Faculty of Geo-information Science and Earth Observation (ITC), Hengelosestraat 99, 7514 AE Enschede, the Netherlands

## ABSTRACT

A technique for estimating clinoptilolite, montmorillonite, and epsomite mineral abundances from a reflectance spectrum of mineral mixtures using spectral deconvolution and a deep neural network is proposed. Sixty-six ternary mineral mixtures were physically prepared with  $<150\text{ }\mu\text{m}$  grain size with different weight percentages of minerals. A combination of normal and skewed Gaussian curves was fitted to the absorption bands at  $1.4\text{ }\mu\text{m}$ ,  $1.9\text{ }\mu\text{m}$ , and  $2.2\text{ }\mu\text{m}$  of the acquired reflectance spectra of these mineral mixtures. Six Gaussian curve parameters with maximum absorption band depth  $\sim 1.9\text{ }\mu\text{m}$ , and wavelength at the maximum band depth, were used (along with mineral abundances) to train multilayer perceptron deep neural network (MLP-DNN) models. Forty-eight models with different DNN architectures and different hyperparameters were trained and the results were validated to find the best models. Winning models were tested using twenty-five samples including fourteen library spectra from RELAB and USGS spectral databases, a spectrum from a different sample, five different amounts of noise-added spectra simulating CRISM (Compact Reconnaissance Imaging Spectrometer for Mars) orbital spectral data, and five mixed spectra derived from linear mixtures of laboratory minerals. The best model was able to predict mineral mixture composition with higher accuracies; three of five montmorillonite and four of the five epsomite library spectra were identified with more than 90% accuracy. However, clinoptilolite samples show less than 50% accuracy and always predicted as mixtures of clinoptilolite and epsomite. This shows the difficulties of distinguishing non-analcime zeolites (e.g., clinoptilolite) from Mg-polyhydrated sulfate minerals, as discussed by authors who mapped hydrous minerals on Mars using hyperspectral image data. Also, the presence of at least  $\sim 10\%$  of montmorillonite in a clinoptilolite-montmorillonite mixture can entirely mask the presence of clinoptilolite in SWIR spectral data. Random artifacts introduced by noise sometime lead to predictions of completely different and incorrect mineral abundances. The study also discusses the possible reasons for the incorrect prediction of mineral abundances and how to overcome these difficulties. Overall, the study shows the advantage of spectral deconvolution with deep neural network for calculating mineral abundance from mixed mineral spectra.

## 1. Motivation and background

As photons enter a mineral, some are absorbed by the grain, some are reflected from the grain surface, and some pass through it. When photons enter an absorbing medium, they are absorbed according to Beer's Law,

$$I = I_0 e^{-kx} \quad (1)$$

where  $I$  is the observed intensity,  $I_0$  is the original light intensity,  $k$  is an absorption coefficient, and  $x$  is the distance traveled through the medium. The equation describes the intensity at a specific wavelength, as the absorption coefficient is wavelength-specific. Differences in absorption coefficients in a certain wavelength range lead to intensity differences, creating absorption bands. Many minerals exposed to solar light wavelengths ( $0.3\text{--}3\text{ }\mu\text{m}$ ) show characteristic absorption bands due to vibrational fundamentals, combinations, and overtones, electronic trans-

sitions, charge transfer, and conduction processes (Hunt, 1977). Very broad absorption bands in the  $\sim 0.3\text{--}0.9\text{ }\mu\text{m}$  wavelength region are typically caused by electronic transitions while the absorption bands in the  $\sim 0.9\text{--}3\text{ }\mu\text{m}$  wavelength region are typically caused by overtones, and combinations of the fundamentals of the absorptions form due to  $\text{OH}^-$ ,  $\text{H}_2\text{O}$ , and  $\text{CO}_3^{2-}$ , which occur at longer wavelengths. The characteristics of these absorption bands (e.g., position, shape, and depth) in reflectance spectra are a powerful tool for remote identification of surface composition on Earth and other planetary bodies.

Based on their spectral characteristics captured by orbital spectral sensors, hydrous minerals, such as smectites, kaolinite, sulfates, carbonates, zeolites, opaline silica, chlorites, serpentine, prehnite, and epidote have been identified on the surface of Mars (Carter et al., 2013; Ehlmann et al., 2009, 2013). Ehlmann et al. (2009) identified the Na-zeolite analcime in the Nili Fossae region on Mars using Compact

\* Corresponding author.

E-mail address: [gayantha\\_kodikara@yahoo.com](mailto:gayantha_kodikara@yahoo.com) (G.R.L. Kodikara).

Reconnaissance Imaging Spectrometer for Mars (CRISM) data. Analcime is the only zeolite group mineral specifically identified on Mars based on its distinctive broad absorption band centered at  $\sim 2.5 \mu\text{m}$  and a weaker absorption at  $\sim 1.8 \mu\text{m}$  (Cloutis et al., 2002; Ehlmann et al., 2009). Carter et al. (2013), Ehlmann et al. (2009), Sun and Milliken (2015), and Wray et al. (2009) have discussed the difficulties associated with identifying other zeolite minerals using spectral data. Identifying other zeolite species is complicated by the lack of diagnostic absorption bands in the visible-shortwave infrared (VIS-SWIR) region (Cloutis et al., 2002), spectral similarity with Mg-polyhydrated sulfates (Ehlmann et al., 2009), and residual atmospheric effects at wavelengths longer than  $2.5 \mu\text{m}$  (Murchie et al., 2007). Carter et al. (2013) noted that the only ways to discriminate polyhydrated sulfates from zeolites are to use the position of the  $2.3\text{--}2.4 \mu\text{m}$  shoulder and the shape of the  $1.9 \mu\text{m}$  absorption. In most studies non-analcime and polyhydrated sulfates are thus commonly categorized as unidentified hydrous phases (e.g., Sun and Milliken, 2015), or as zeolite and sulfate group (e.g., Carter et al., 2013; Wray et al., 2009).

Gendrin et al. (2005) identified hydrated sulfates including kieserite, polyhydrated sulfate, and gypsum on light-toned layered terrain in Valles Marineris, Margaritifer Sinus, and Terra Meridiani on Mars, using the image bands in the wavelength region between  $1.3$  and  $2.5 \mu\text{m}$  of OMEGA (Observatoire pour la Minéralogie, l'Eau, les Glaces et l'Activité) hyperspectral data. It is important to note that for most of the locations where sulfates are identified, monohydrated sulfate layers coexist with polyhydrated sulfates layers in an interbedded sulfate stratigraphy (Roach et al., 2009; Wang et al., 2016), or sulfate minerals and clays occur together (e.g., Milliken et al., 2010; Weitz et al., 2015; Wray et al., 2011). On Earth, evaporitic sulfate minerals commonly occur together with detrital clays and/or authigenically precipitated clay minerals in modern and ancient saline lakes and playa environments (Warren, 2016). Zeolites are the most common authigenic silicate minerals in saline, alkaline lakes associated with detrital or authigenic clay minerals (Hay, 1966). Therefore, it is not unexpected that the same may be true for Mars, though the zeolites have not yet been reported in Martian meteorites or in data from in situ landers or rovers. Orbital reflectance spectroscopy provides an effective way to map the spatial distribution of these minerals to assess the activity, timing, duration, and extent of aqueous processes over Martian history. However, questions remain about how reliably these mineral components can be detected and their relative abundances estimated, given the difficulties observed in previous studies.

The process of identifying minerals and determining their quantitative abundances from the reflectance spectra of mineral mixtures is not straightforward. Efforts to identify minerals and their abundances are hindered by the complexities introduced by particle size effects, variations in viewing and illumination geometry, surface roughness, and regolith or weathering alteration on reflectance spectra (Mustard and Pieters, 1989). Multiple theoretical and empirical approaches have been introduced to estimate mineral abundances from the reflectance spectra of mineral mixtures under laboratory conditions and on planetary surfaces. Radiative transfer models (RTMs) are one of the most common theoretical models used to describe how light intensity changes as it enters, interacts with, and exits a specific medium (Robertson et al., 2016). Hapke (Hapke, 1981, 1993) and Shkuratov (Shkuratov et al., 1999) RTM models have been commonly used for modeling spectra of laboratory mineral mixtures (e.g., Cahill et al., 2010; Liu et al., 2015; Robertson et al., 2016; Stack and Milliken, 2015) and planetary surfaces (e.g., Cahill et al., 2009; Trang and Lucey, 2019). Hapke's model is designed for intimate mixtures of particulates, while the Shkuratov RTM treats particles as a one-dimensional layer (Robertson et al., 2016). Stack and Milliken (2015) examined the VNIR reflectance properties of a suite of binary mineral mixtures containing epsomite mixed with varying proportions of Fe, Mg, and Al-smectites, and assessed the ability of linear and non-linear (Hapke) models to reproduce spectra of these mineral mixtures. Robertson et al. (2016) assessed the efficacy of the Hapke and Shkuratov RTMs for estimating mineral abundances from

gypsum-montmorillonite binary mineral mixtures. RTMs are useful as diagnostic tools for mixtures of specific minerals, though they are limited to applications that only involve the minerals studied (Sunshine et al., 1990).

Curve fitting is the classic empirical approach to model reflectance spectra and resolve single absorption bands within complex absorption features. The reflectance spectra can be modeled by a linear combination of overlapping absorption bands superimposed onto a background continuum (Clark and Roush, 1984). Because of that, curve fitting methods have been extensively used to decompose reflectance spectra of mineral mixtures to identify their constituent minerals both in laboratory mineral mixtures (e.g., Noble et al., 2006; Parente et al., 2011; Sunshine et al., 1990) and planetary surfaces (e.g., Brown, 2006; Kodikara et al., 2016; Parente et al., 2011). Spectral deconvolution resolves spectra into individual absorption bands with discrete mathematical distributions. The absorption bands can be modeled using Gaussian, modified Gaussian, Lorentz, or Voight (mixed Gaussian-Lorentz) curves (Brown, 2006; Clark, 1981; Sunshine et al., 1990). These curves are all symmetrically shaped and decay from a central peak, and different decay rates may represent different physical processes (Brown, 2006). Curve fitting of spectra can estimate the central wavelength, width, amplitude, and asymmetry of the absorption band, and is typically achieved using an iterative least square method (Brown, 2006). The modified Gaussian model (MGM), developed by Sunshine et al. (1990), provides an accurate mathematical description of the shape of isolated electronic transition absorption bands, and Sunshine and Pieters (1993) noted that this can estimate modal abundances from spectra of unknown pyroxene mixtures without the use of end member spectra. Roush et al. (2015) used four absorption parameters (center, width, depth, and asymmetry) of reflectance spectra from saponite + montmorillonite with pyroxene, and saponite with palagonitic soil mixtures, in the wavelength region of  $2.1\text{--}2.3 \mu\text{m}$  to extract the clay abundances from the mixed mineral spectra. Asymmetry parameters range from  $0$  to  $\infty$ , and  $<1$  indicates the band is wider on the short-wave side while  $>1$  indicates the band is wider on the long-wave side. An asymmetry value of  $1$  indicates a symmetrical absorption band (Roush et al., 2015). The Roush et al. (2015) study found that the absorption band depth is the best feature to use to determine saponite/montmorillonite abundance in the mixtures.

Deep learning (DL) methods, a subfield of machine learning (ML), are representation-learning methods with multiple levels of representation (layers), obtained by a composite of simple non-linear modules that each transform the representation at one level (from input layer) into a representation at a higher, slightly more abstract levels (hidden layers to output layer) (LeCun et al., 2015). The key feature of DL is that these layers of features are not designed by humans, they are learned automatically from exposure to training data using a learning algorithm. DL is very good at discovering intricate structures in high-dimensional data and therefore it is used in many fields, including science, image recognition, speech recognition, business, natural language processing, robotics, etc. A review of deep learning and its evolution can be found in LeCun et al. (2015) and Schmidhuber (2015), respectively. Kodikara and McHenry (2020) examined the ability of ML algorithms, adopting 9 ML algorithms representing linear, non-linear, classification trees, and rule-based models, to determine the physical and mineralogical properties of lunar soil using the reflectance spectra of lunar soils.

Here we assess the efficacy of a combination of spectral deconvolution and deep learning to estimate mineral abundances of zeolite, Mg-sulfate, and montmorillonite mixtures using their reflectance spectra. The main idea of this study is to understand how well zeolite minerals can be identified using DL methods and spectral data. Montmorillonite and Mg-sulfate were selected as the other end members for two main reasons. 1) As discussed earlier, previous studies showed that zeolite minerals are difficult to distinguish from Mg-sulfate minerals using orbital spectral data. This study assesses the capability of the DL method to distinguish zeolite and Mg-sulfate spectra. 2) Zeolites and Mg-sulfate minerals are often found associated with smectite clay minerals in na-

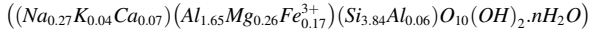
ture and therefore this study also assesses the advancement of DL method for identification and calculation of relative mineral abundances in these mineral mixtures. This is especially important as it addresses the tendency of clays to dominate the spectra of mixtures, disproportionate to their relative abundances, effectively “masking” the presence of less spectrally dominant phases such as zeolites. By considering all three end members, this study also aims to help determine whether montmorillonite/Mg-sulfate mixtures can be distinguished from montmorillonite/zeolite mixtures using their reflectance spectra, which could help distinguish between more neutral to acidic (sulfate-bearing) and alkaline (zeolite-bearing) evaporitic environments on Mars. Our study was limited to the absorption features caused by vibrational overtones and combinations in the reflected light portion of the spectrum within the 1.4 to 2.5  $\mu\text{m}$  region.

The rest of the paper is organized as follows: Section 2 discusses the details of sample preparation, spectral acquisition, and preprocessing of the collected spectral data. Section 3 outlines the identification of spectral features for Gaussian curve deconvolution, parameter estimation, and feature selection. Section 4 discusses the selection of the best deep learning model using its hyperparameters and validation process. Section 5 reports an accuracy assessment using test data. Section 6 concludes this study. The entire study was conducted using several python modules (numpy, math, lmfit, matplotlib, and pytorch) implemented in Rstudio IDE (integrated development environment) (<https://www.rstudio.com>) installed on MacBook Air (1.6 GHz Dual-Core i5, 4 GB 1600 MHz DDR3). An open source machine learning framework PyTorch (<https://pytorch.org/>) was used to build deep learning models.

## 2. Spectral analysis

### 2.1. Sample preparation

The end member minerals selected for this study are clinoptilolite, montmorillonite, and epsomite. Clinoptilolite ( $(Na, K, Ca)_{2-3}Al_3(Al, Si)_2Si_3O_{36}\cdot 12H_2O$ ) was purchased from [www.Kelp4less.com](http://www.Kelp4less.com), montmorillonite



was purchased from Wards collection (No.46E0438), which was collected from Panther Creek, Colorado. The commercial USP grade synthetic salt Epsomite ( $MgSO_4\cdot 7H_2O$ ) was also purchased from a local store. These samples were individually ground and dry-sieved to a size fraction of  $<150 \mu\text{m}$ . The purity of these mineral end members was tested using a Bruker D8 Focus X-ray diffraction (XRD) system. XRD patterns were compared against the ICDD PDF-2 (International Center for Diffraction Data Powder Diffraction File) library using Bruker's EVA software. The montmorillonite sample contains minor amounts of albite and quartz, while the clinoptilolite sample contains minor cristobalite. The epsomite sample contains a minor amount of hexahydrite, most likely due to the dehydration of epsomite. Epsomite transforms readily to hexahydrite by loss of extra-polyhedral water at 298 K and  $\sim 50\text{--}55\%$  relative humidity conditions (Vaniman et al., 2004). Since more than 90% of each sample is represented by the major mineral of interest, these samples were considered as “end members” for the purpose of this study.

Sixty-six ternary mineral mixtures, each totaling 2.00 g, were prepared. The mineral abundances (weight percentage) of each end member mineral in each mixture are represented by the blue points on the ternary plot in Fig. 1, and Table S1 in the supplementary document. Mineral proportions for each sample were weighed separately, accurate to 0.005 g, and then mixed well to ensure homogeneous mixing. Samples were prepared under ambient laboratory conditions.

### 2.2. Spectral acquisition

The VIS-SWIR reflectance spectrum of each mineral mixture was

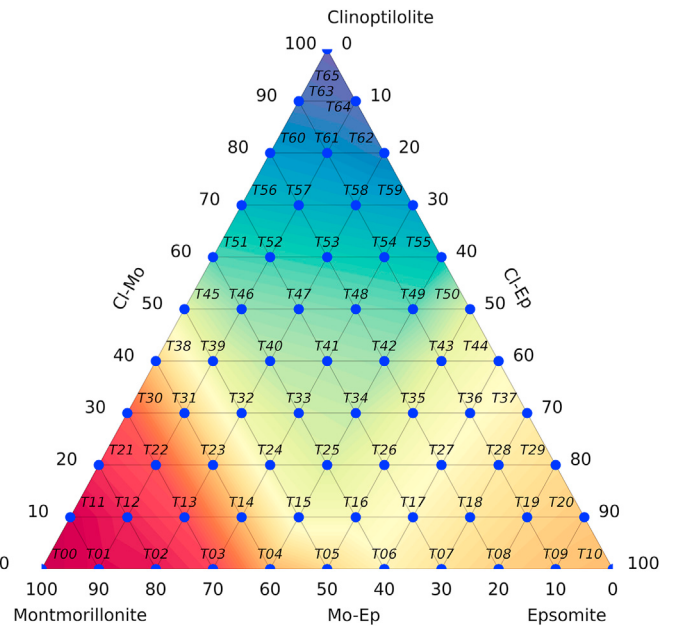


**Fig. 1.** Schematic ternary diagram for mixtures of clinoptilolite, montmorillonite and epsomite. Blue points show the sample points of physical mineral mixtures prepared to collect reflectance spectra. The sample ID for each mixture is shown near the sample point.

collected using a TerraSpec Halo reflectance spectrometer (350–2500 nm spectral range with a spectral resolution of 3 nm @ 700 nm, 9.8 nm @ 1400 nm, and 8.1 nm @ 2100 nm, and high SNR: 9000:1 @ 700 nm and 1400 nm, 4000:1 @ 2100 nm) at the University of Colorado under ambient laboratory conditions. The spectral ID of each mineral mixture is the same as the sample ID shown in Fig. 1. Reflectance spectra of mineral end members (spectral endmembers) are shown in Fig. 2.

In hydrous minerals, water molecules occur in different contexts. They can be bound to the interlayer surface, as interlayer cations as in montmorillonite, or can occur singly or in clusters forming an essential part of the crystal lattice as in various hydrates in Mg-sulfates (e.g., epsomite and hexahydrite), occupying specific sites in the crystal structure without being essential to its structure, as in clinoptilolite, or physically adsorbed on the surfaces of mineral grains (Bishop et al., 1994; Hunt and Salisbury, 1970). Water molecules have three fundamental vibrational modes, the symmetric O–H stretch, the asymmetric O–H stretch, and the H–O–H bend. Absorption band assignments for clinoptilolite, montmorillonite, and epsomite are shown in Table 1.

It is important to note that due to relatively high iron impurities ( $\sim 1.7 \text{ wt\% } Fe_2O_3$ ) in the clinoptilolite sample, the reflectance spectrum of clinoptilolite shows a spectral slope on the left side of left shoulder of the 1.4  $\mu\text{m}$  absorption band due to the broad absorption band near 0.9  $\mu\text{m}$  formed due to the  $Fe^{2+}$  crystal field transition. While care was taken to handpick the purest mineral chips to grind, some iron oxide remains. The dominant absorption bands between 1.2 and 2.5  $\mu\text{m}$  are formed mainly due to vibrational processes (Table 1), and therefore iron content of the sample does not affect the current study.

The original spectra of mineral mixtures are shown in Fig. 3 (a). The spectra show different intensity variations making it difficult to visually analyze the spectra to select which absorption bands are best for determining relative mineral abundances. Therefore, these spectra were corrected using a multiplicative scattering correction algorithm (MSC) (Geladi et al., 1985). MSC compensates for the multiplicative effects caused by light scattering effects and changes in path length. The MSC corrected spectra ( $X_{MSC}$ ) are shown in Fig. 3 (b). The MSC corrected spectra were calculated using,

$$X_{MSC} = (x - a) / b \quad (2)$$

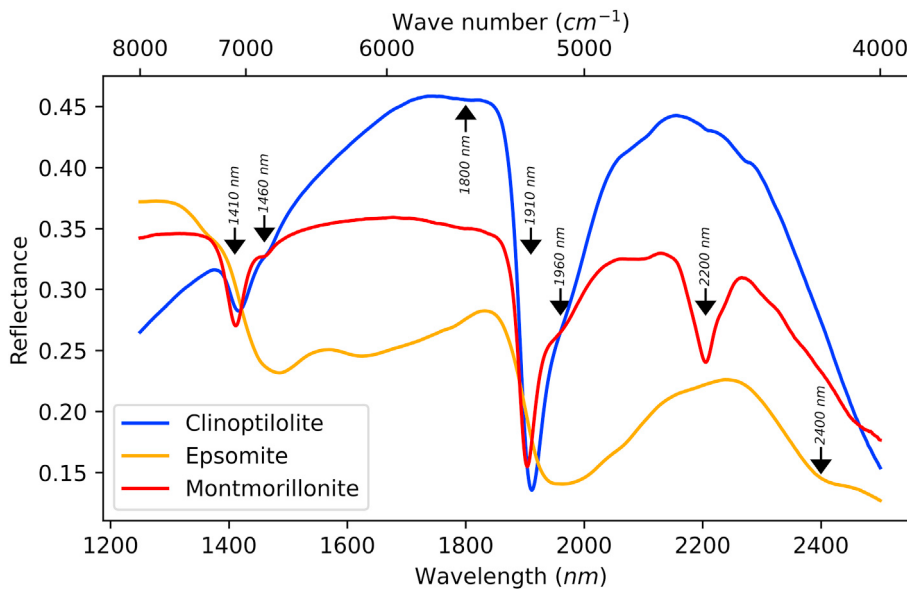


**Fig. 2.** Reflectance spectra of mineral end members (spectral endmembers) used in this study.

**Table 1**

Absorption band assignment for clinoptilolite, montmorillonite and epsomite (sources: Bishop et al., 1994; Clark, 1995; Cloutis et al., 2002; Cloutis et al., 2006; Gendrin et al., 2005; Hunt and Salisbury, 1970).

Wavelength $\mu\text{m}$	Assignment	Mineral
1.41	$H_2O$ stretch + first overtone of $H_2O$ bend	CLI, MON
1.46	$H_2O$ stretch + second overtone of $H_2O$ bend	CLI, EPS, MON
1.80	Symmetric or asymmetric $H_2O$ stretch	CLI
1.91	$H_2O$ stretch + $H_2O$ bend	CLI, EPS, MON
1.97	$H_2O$ combinations	EPS
2.20	$OH$ stretch + bend ( $Al_2 - OH$ )	MON
2.40	$(SO_4)^{2-}$ stretch	EPS

Note: CLI = Clinoptilolite, EPS = Epsomite, and MON = Montmorillonite.

where  $x$  = the spectrum of a sample.

$a$  and  $b$  were estimated using ordinary least-squares regression of spectrum  $x$  versus  $\bar{x}$ , using equation (3).

$$x = a + b\bar{x} + e \quad (3)$$

where  $\bar{x}$  = spectrum of the “ideal” sample (mean spectrum in this case),  $e$  = residual spectrum.

### 2.3. Selection of spectral features

The spectra of binary mineral mixtures were used to find which important absorption bands vary with mineral abundance (Fig. 4). The letter C in the legend indicates clinoptilolite, M indicates montmorillonite, and E indicates epsomite. Two integers after each letter indicate the respective weight proportion of each mineral on a scale of 10. This figure shows that absorption bands around  $1.4 \mu\text{m}$ ,  $1.9 \mu\text{m}$ , and  $2.2 \mu\text{m}$  change with their mineral abundances. The shape of the absorption bands at  $1.4 \mu\text{m}$  and  $1.9 \mu\text{m}$  does not vary much with changes in mineral weight proportion for the clinoptilolite-montmorillonite binary mineral mixture (Fig. 4a), while the depth and shape of these absorption bands varies greatly for the clinoptilolite-epsomite and epsomite-montmorillonite binary mineral mixtures due to broad spectral features of epsomite. The absorption band at  $2.2 \mu\text{m}$  increases with increased montmorillonite as expected for both the clinoptilolite-montmorillonite (Fig. 4a) and montmorillonite-epsomite (Fig. 4c) binary mineral mixtures. Based on the spectral characteristics of the absorption bands

discussed here, three wavelength regions covering absorption bands at  $1.4 \mu\text{m}$ ,  $1.9 \mu\text{m}$ , and  $2.2 \mu\text{m}$  were selected and referred to here as F1 (feature 1), F2 (feature 2), and F3 (feature 3), respectively. The wavelength ranges for features F1, F2, and F3 were determined based on the extreme convex points on either side of the respective feature shoulders. To compare and implement the curve fitting to these features, a piecewise straight-line continuum was removed from the spectra across the F1, F2, and F3 regions (Fig. 5). The continuum is a mathematical function used to isolate a particular absorption feature for analysis of a spectrum (Clark and Roush, 1984).

### 3. Spectral deconvolution

To represent mathematically the reflectance spectra of selected wavelength regions as linear combinations of absorption bands that occur around discrete energies, it is necessary to use a Gaussian model of absorption bands in log reflectance and energy space (Sunshine et al., 1990). Also, the overlapping absorption bands are additive when measured in absorbance (Brown, 2006). Therefore, the reflectance spectra were converted to apparent absorbance by taking the logarithm of the reflectance,

$$\text{apparent absorbance} = \log_{10}(\text{reflectance}) \quad (4)$$

The original spectra were recorded in wavelength space; therefore, they were converted to energy space in  $\text{cm}^{-1}$  (wavenumbers). Converting to energy space also eliminates the asymmetry due to display on a constant interval wavelength abscissa (Rossman, 1988).

$$\text{frequency } (\text{cm}^{-1}) = \frac{10000}{\text{wavelength}(\mu\text{m})} \quad (5)$$

The underlying assumption of the Gaussian model is that absorption bands observed in VIS-SWIR spectra are composed of absorption features that are inherently Gaussian in shape. If this is true, these spectral features can be resolved into absorption bands by curve fitting using Gaussian distributions (Sunshine et al., 1990). Roush and Singer (1986) pointed out that a Gaussian deconvolution should produce a unique fit for a given mineral under certain reasonable constraints. Even if it is not firmly tied to a physical mechanism, this can provide some useful information to analyze absorption bands (Sunshine et al., 1990).

Several curve fitting algorithms including Gaussian, Lorentzian, and Voigt were tested using the lmfit python module, and the Gaussian

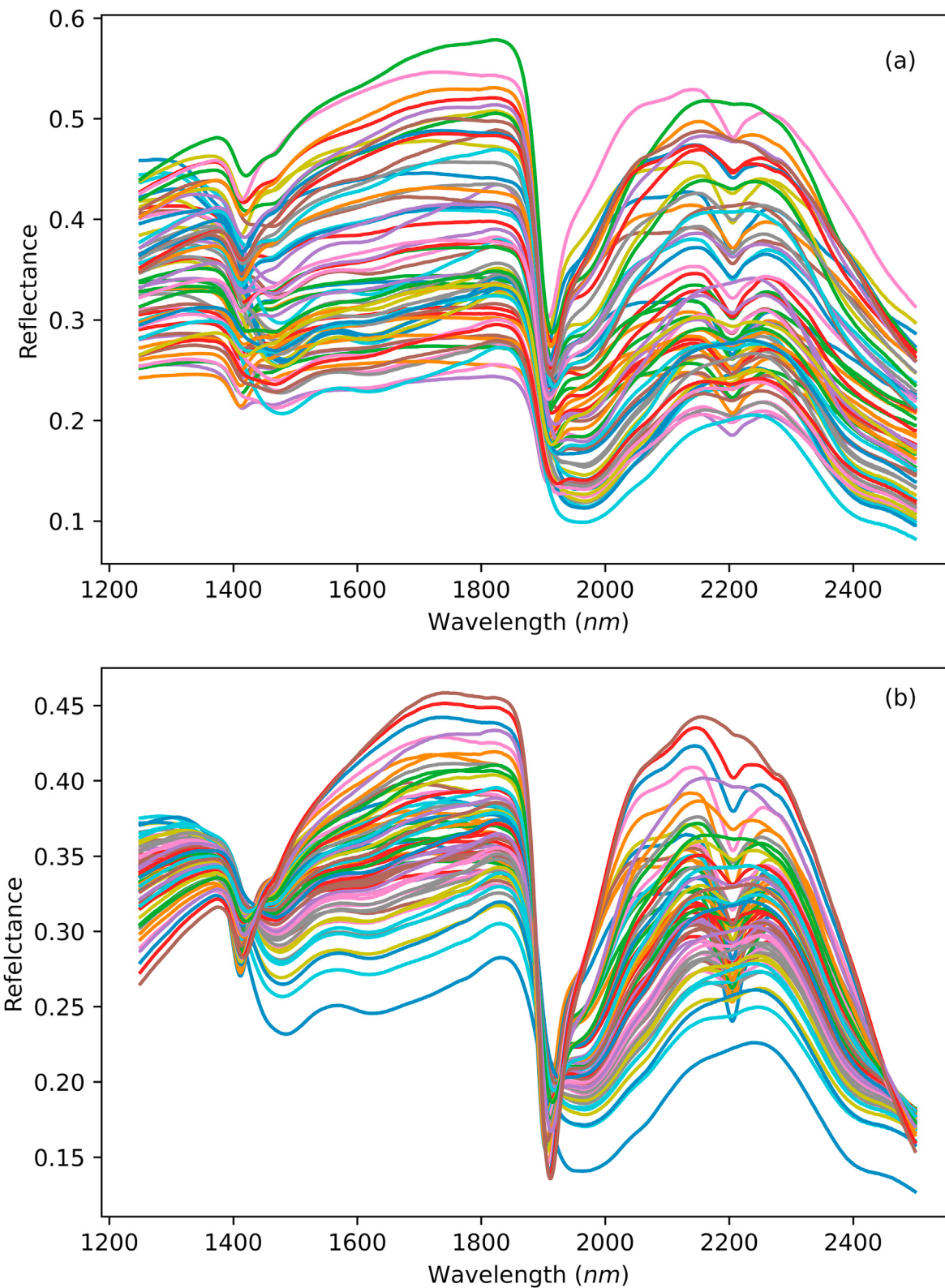


**Fig. 3.** Original mineral mixture spectra (a) and after applying the multiplicative scatter correction (b).

models provide a better fit for the selected absorbance regions of mineral end members and mixtures (Figure S1 in supplementary document). A Gaussian distribution in a random variable  $x$ ,  $f(x; A, \mu, \sigma)$ , can be expressed in terms of its amplitude (strength of the peak);  $A$ , center (centeroid of the curve);  $\mu$ , and sigma (width of the peak);  $\sigma$ .

$$f(x; A, \mu, \sigma) = \frac{A}{\rho\sqrt{2\pi}} e^{[-(x-\mu)^2/2\sigma^2]} \quad (6)$$

A Levenberg-Marquardt (L-M) algorithm (Levenberg, 1944; Marquardt, 1963) was used to find the best fit curve. Brown (2006) used the L-M algorithm for spectral curve fitting in the shortwave infrared (SWIR)

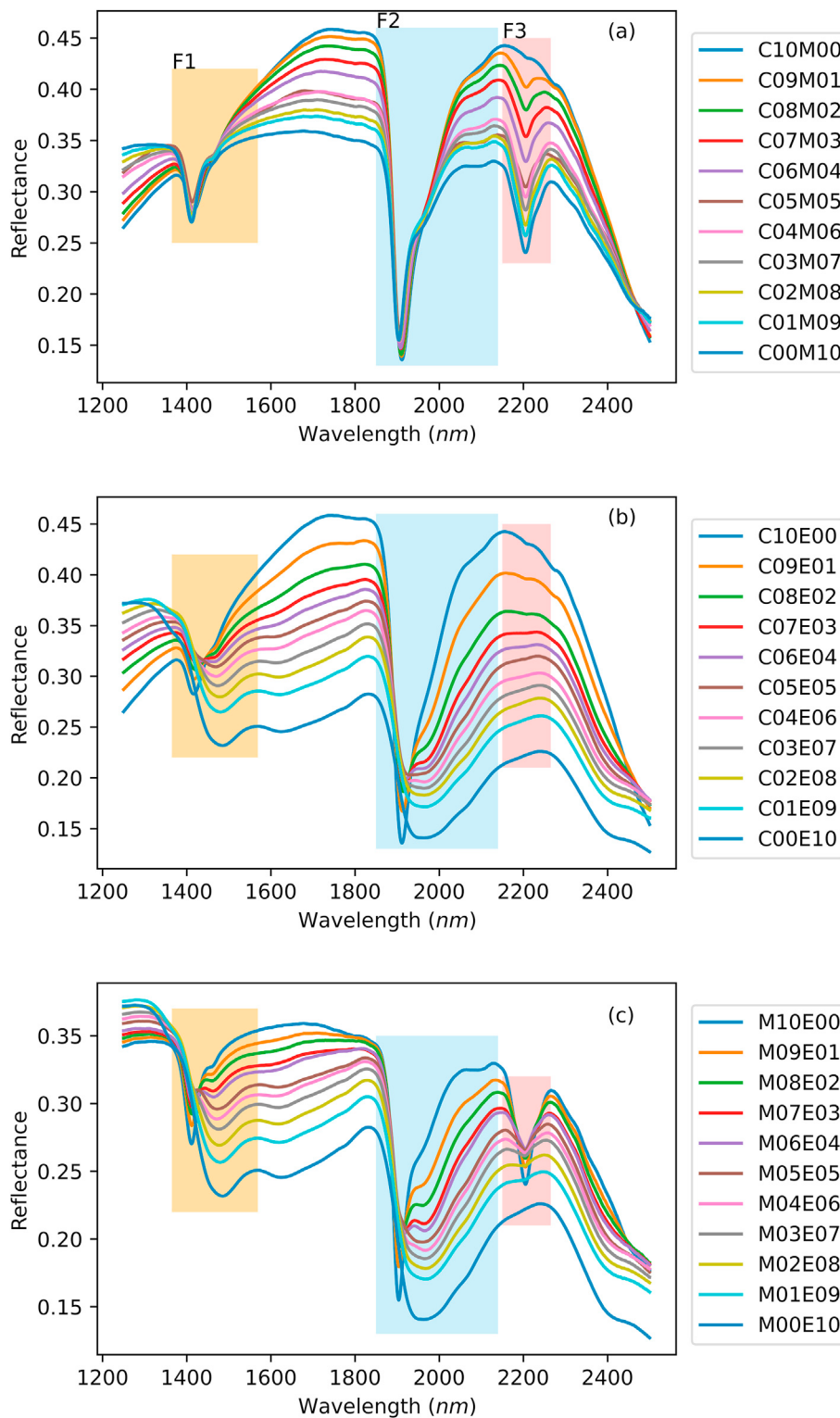


**Fig. 4.** Binary mineral mixtures showing absorption feature variations associated with varied mineral abundances. Each subplot shows a binary mineral mixture: (a) clinoptilolite - montmorillonite, (b) clinoptilolite - epsomite, and (c) montmorillonite - epsomite. F1, F2, and F3 are the wavelength regions of the absorption features selected for this study. Letter C in the legend indicates clinoptilolite, M indicates montmorillonite, and E indicates epsomite. Two integers after each letter indicate the mineral weight proportions on a 10 point scale.

region. Parente et al. (2011) adopted the L-M and Total Inversion (Tarantola and Valette, 1982) methods for curve fitting modeling of reflectance spectra for Martian meteorites and CRISM spectral image data. They found that both L-M and total inversion methods perform similarly on low-noise spectra, though L-M is more stable when its parameters are varied. The main advantage of the L-M algorithm in curve fitting is that uncertainties of the model parameters can be included in the form of ranges of values. The range of initial values for the width, strength, and

centers for each feature were provided at first and then the fitting procedure iteratively adjusts these parameters until a negligible improvement in the overall fit is obtained. The input value ranges, initial values for iteration and output Gaussian curve parameter values for the three end member minerals and T53 mineral mixture are shown in Table 2. The complete dataset can be found in the supplementary documents.

Two normal Gaussian curves appear to be sufficient to achieve a good least squares fit for Feature 1 (examples in Fig. 6a, d, g, and j), though

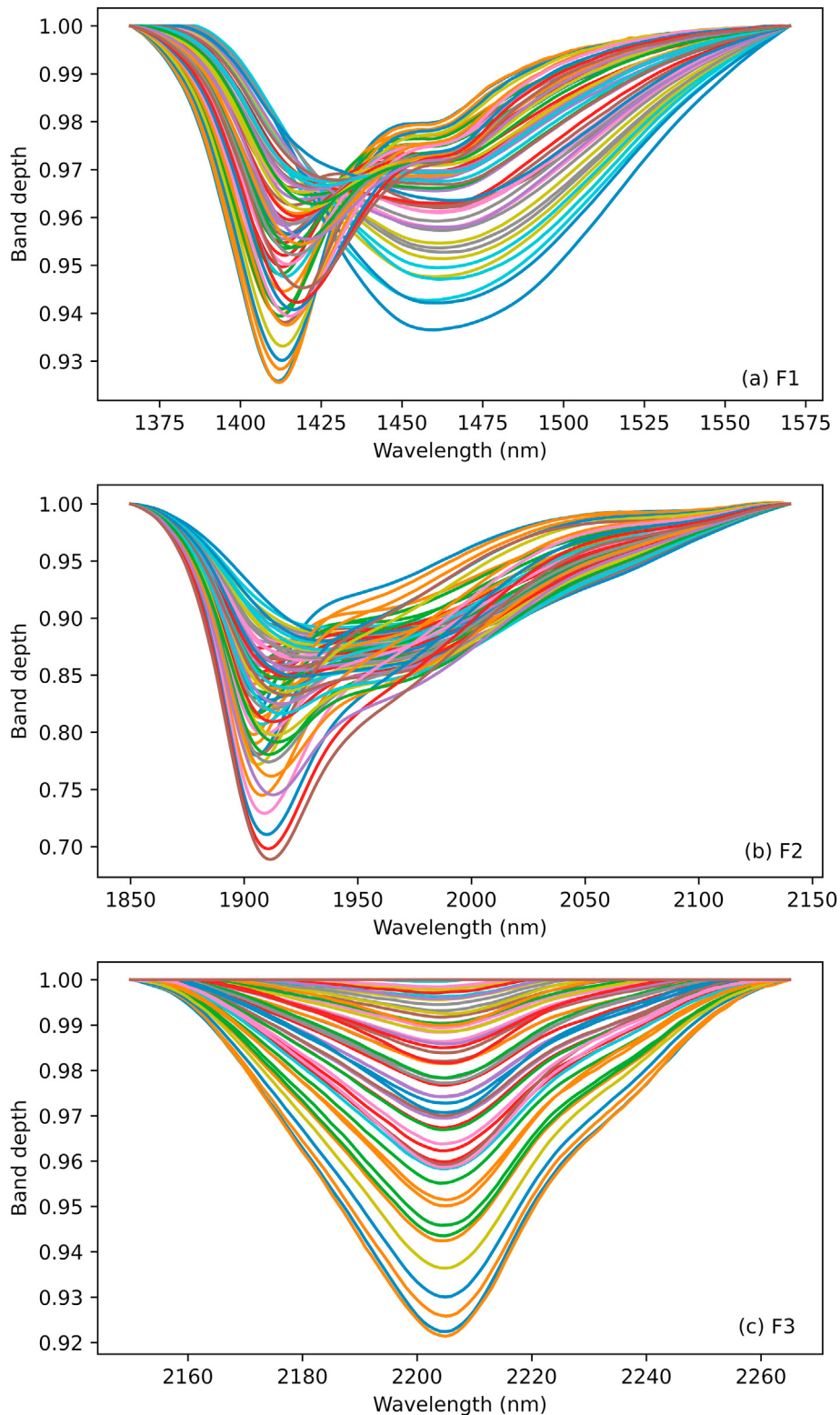


**Fig. 5.** Continuum removed spectra across the (a) F1, (b) F2, and (c) F3 wavelength regions.

Feature 2 is best represented by combining a normal Gaussian curve and a skewed Gaussian curve (Fig. 6b, e, h, and k). Feature 3 can be represented by a normal Gaussian curve (Fig. 6c, i, and l).

The Skewed Gaussian model can be represented by

$$f(x; A, \mu, \sigma, \gamma) = \frac{A}{\rho\sqrt{2\pi}} e^{-[(x-\mu)^2/2\sigma^2]} \left\{ 1 + \operatorname{erf} \left[ \frac{\gamma(x-\mu)}{\sigma\sqrt{2}} \right] \right\} \quad (7)$$

where  $A$  = amplitude,  $\mu$  = center,  $\sigma$  = width of the peak,  $\gamma$  = skewness, and  $\operatorname{erf} \left[ \frac{\gamma(x-\mu)}{\sigma\sqrt{2}} \right]$  is the error function.

The amplitude of the peak ( $A$ ), central frequency of the peak ( $\mu$ ), width of the peak ( $\sigma$ ) and skewness ( $\gamma$ , in the case of skewed Gaussian model) were calculated for all fitted Gaussian curves of Features F1, F2, and F3. The skewness value is  $> 0$  for the left skewed and  $< 0$  for the right

**Table 2**

Input parameters used for spectral deconvolution model and output Gaussian parameters of three end members (T00, T10, and T65) and mineral mixture sample T53. Input parameters for the band center (CNT) were given as a range and the minimum value of amplitude (AMP) and sigma (SGM) was also given. Initial (guessed) values were given in each case and listed as a set value in the table. Prefix G1\_ represent the Gaussian curve 1 while G2\_ represents the Gaussian curve 2. AMP = amplitude, CNT = center, SGM = sigma, and GMA = gamma.

Feature	Range	Input Parameters							
		Gaussian Curve 1				Gaussian Curve 2			
		G1_AMP	G1_CNT	G1_SGM	G1_GMA	G2_AMP	G2_CNT	G2_SGM	
F1	Min	0.00020	6.50	0.10		0.0010	7.000	0.010	
	Max		6.90				7.200		
	Set	0.00195	6.60	0.16		0.0063	7.082	0.075	
F2	Min	0	4.51	0		0	5.100	0	
	Max		5.50				5.300		
	Set	0.01630	5.12	0.20		0.0063	5.250	0.070	
F3	Min	0	4.48	0					
	Max		4.58						
	Set	0.00040	4.50	0.01					
Spectra	Feature	Output Parameters							
		G1_AMP	G1_CNT	G1_SGM	G1_GMA	G2_AMP	G2_CNT	G2_SGM	
T00	F1	0.003392	6.900000	0.160284		0.004993	7.092290	0.069900	
	F2	0.006067	5.283195	0.050893	-1.650796	0.010043	5.136767	0.117750	
	F3	0.003367	4.538489	0.040158					
T10	F1	0.012222	6.788419	0.171779		0.001269	7.000000	0.077828	
	F2	0.014711	5.066074	0.163020	-0.742514	0.007234	5.183232	0.083374	
	F3	0	0	0					
T65	F1	0.005326	6.895930	0.164633		0.003012	7.061079	0.073455	
	F2	0.030473	5.262636	0.202836	-2.947525	0.008820	5.242384	0.041260	
	F3	0.000003	4.541803	0.007354					
T53	F1	0.005003	6.870841	0.166904		0.002020	7.069470	0.070381	
	F2	0.023132	5.211755	0.211924	-2.482925	0.006932	5.242534	0.047168	
	F3	0.000529	4.539864	0.033297					

skewed curves. Since the absorption bands at F1 (near  $1.4 \mu\text{m}$ ) and F2 (near  $1.9 \mu\text{m}$ ) are composed of multiple, overlapping molecular water features, the band shape, band depth and band strength are all important to find the relationship between constituent mineral abundance and their spectra.

Calculated Gaussian parameters for F1 are shown in Fig. 7. This shows that the amplitude and center wavelength of Gaussian curve 1 (F1G1\_AMP; plot a, and F1G1\_CNT; plot b, respectively) and Gaussian curve 2 (F1G2\_AMP; plot d, and F1G2\_CNT; plot e) show a relatively clear general trend across the ternary diagram. The amplitude of Gaussian curve 1 increases towards epsomite, while the amplitude of Gaussian curve 2 increases towards montmorillonite. The center frequencies of Gaussian curves are converted to wavelength space for easy reference. The center wavelength of both Gaussian curve 1 (F1G1\_CNT, plot b) and curve 2 (F1G2\_CNT, plot e) of F1 increase towards epsomite. The width of the peaks ( $\sigma$ ) of Gaussian curve 1 (F1G1\_SGM, plot c) and Gaussian curve 2 (F1G2\_SGM, plot f) of F1 do not show a general trend across the plot.

Fig. 8 shows the amplitude of Gaussian curve 1 of F2 (F2G1\_AMP, plot a), the maximum band depth of F2 (F2BD\_MAX; band depth calculated using continuum removed spectra, plot b), the wavelength at the maximum band depth (F2WL\_MAX, plot c), and amplitude of Gaussian curve 1 of F3 (F3G1\_AMP, plot d). This shows that the maximum band depth of F2 increases towards epsomite while the wavelength of the maximum band depth increases towards clinoptilolite. Gaussian curve 1 of F3 increases towards montmorillonite as expected. The rest of the parameters do not show clear patterns across the ternary plots (Figure S2 and S3 in supplementary document).

This shows that some of the Gaussian curves and spectral parameters have clear general trends in the ternary plots while others do not. Therefore, eight parameters that depict clearer patterns in the ternary diagrams were selected as input parameters for the DL model. The selected parameters are F1G1\_AMP, F1G1\_CNT, F1G2\_AMP, and F1G2\_CNT shown in Fig. 7, and F2G1\_AMP, F2BD\_MAX, F2WL\_MAX, and F3G1\_AMP shown in Fig. 8. The process of selecting the most useful features to train among existing features is called feature selection in the

ML realm. Feature selection is an effective way to identify the important features in a dataset and discard others as irrelevant and redundant. Irrelevant and redundant features in the training dataset can result in highly unstable models and poor performance (e.g., [Kodikara and McHenry, 2020](#)).

#### 4. Deep learning

Picking the right deep neural network (DNN) architecture is more an art than a science, while there are some best practices and principles, only practice can help to select the best DNN architecture for a specific use ([Chollet and Allaire, 2018](#)). The Multilayer Perceptrons (MLP) neural network, the simplest deep neural network, consisting of a stack of many fully connected (also called densely connected) layers on top of each other, was adopted for this study. Each layer feeds into the layer above it, starting with the input layer into which we feed the data. It may consist of one or more hidden layers and the uppermost layer is the output linear predictor. Fig. 9 shows the MLP with eight inputs, three outputs, and two hidden layers containing six units per layer. Hidden layers can be explained by,

$$H_1 = \sigma_1(XW_1 + b_1) \quad (8)$$

Where,  $H_1$  is the first hidden layer that can be denoted by matrix  $H_1 \in \mathbb{R}^{n \times h}$ ,  $H$  is a matrix with a minibatch of  $n$  examples with  $h$  hidden units. The matrix  $X$  input layer has  $n$  examples with  $d$  input features ( $X \in \mathbb{R}^{n \times d}$ ). Since hidden and output layers are fully connected, first hidden weights and bias can be represented by  $W_1 \in \mathbb{R}^{d \times h}$  and  $b_1 \in \mathbb{R}^{1 \times h}$ , respectively. The weights (also called trainable parameters) contain the information learned by the network when exposed to training data. A nonlinear activation function for hidden layer 1 is denoted by  $\sigma_1$ . Activation functions decide whether a neuron should be activated or not based on the calculated weighted sum after adding bias. Two of the most popular activation functions, ReLU and Sigmoid, were tested. ReLU (rectified linear unit) provides a very simple nonlinear transformation for

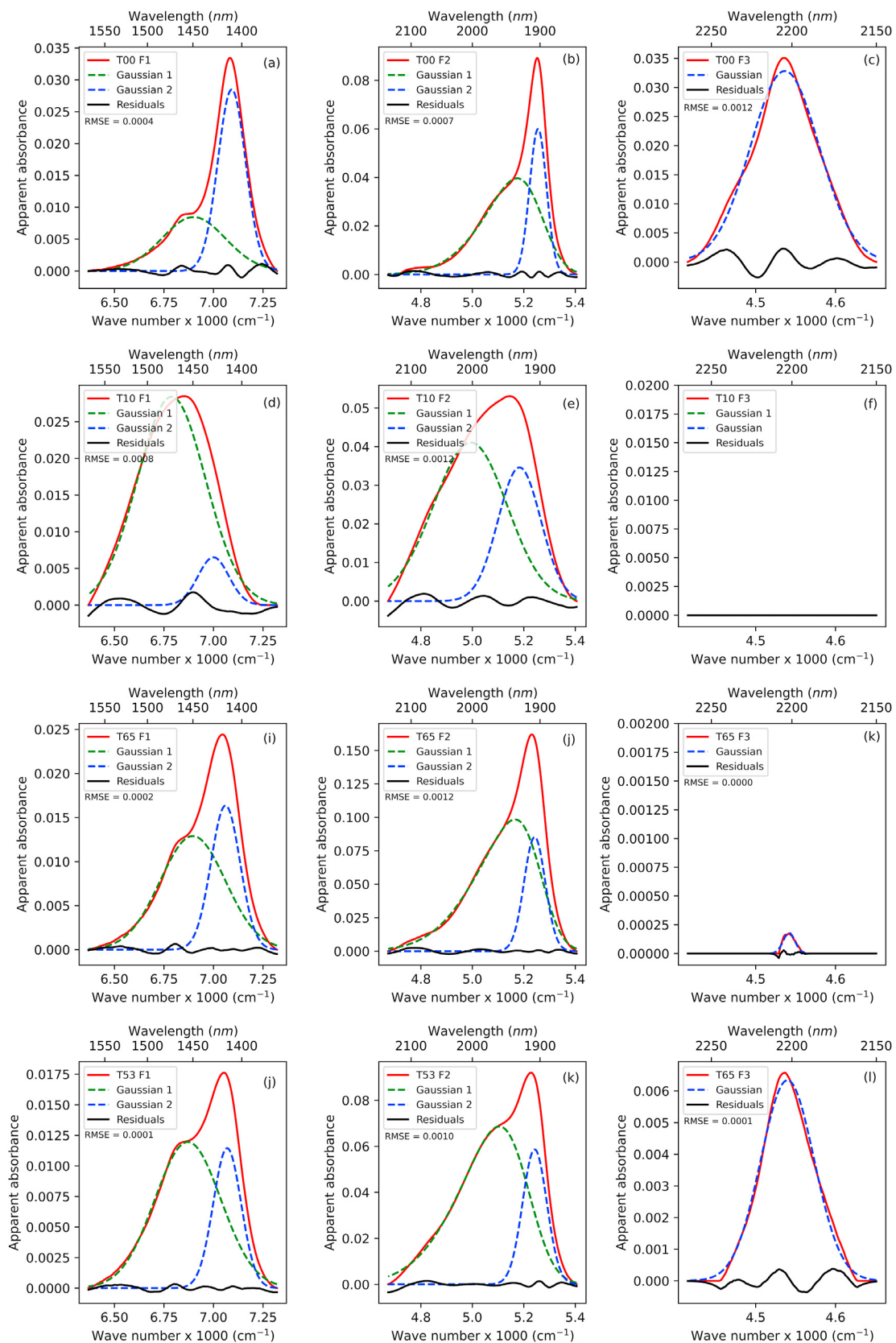


**Fig. 6.** Example of Gaussian curve fitting for F1 (a), F2 (b), and F3 (c) of sample T00 (montmorillonite), F1 (d), F2 (e), and F3 (f) of sample T10 (epsomite), F1 (g), F2 (h), F3 (i) of sample T65 (clinoptilolite), and F1 (j), F2 (k), and F3 (l) of mineral mixture T53 (60 percent clinoptilolite, 20 percent montmorillonite, and 20 percent epsomite). This shows that F1 can be represented by two normal Gaussian curves, while F2 can be represented by a normal and a skewed Gaussian curve. F3 is represented by one normal Gaussian curve.

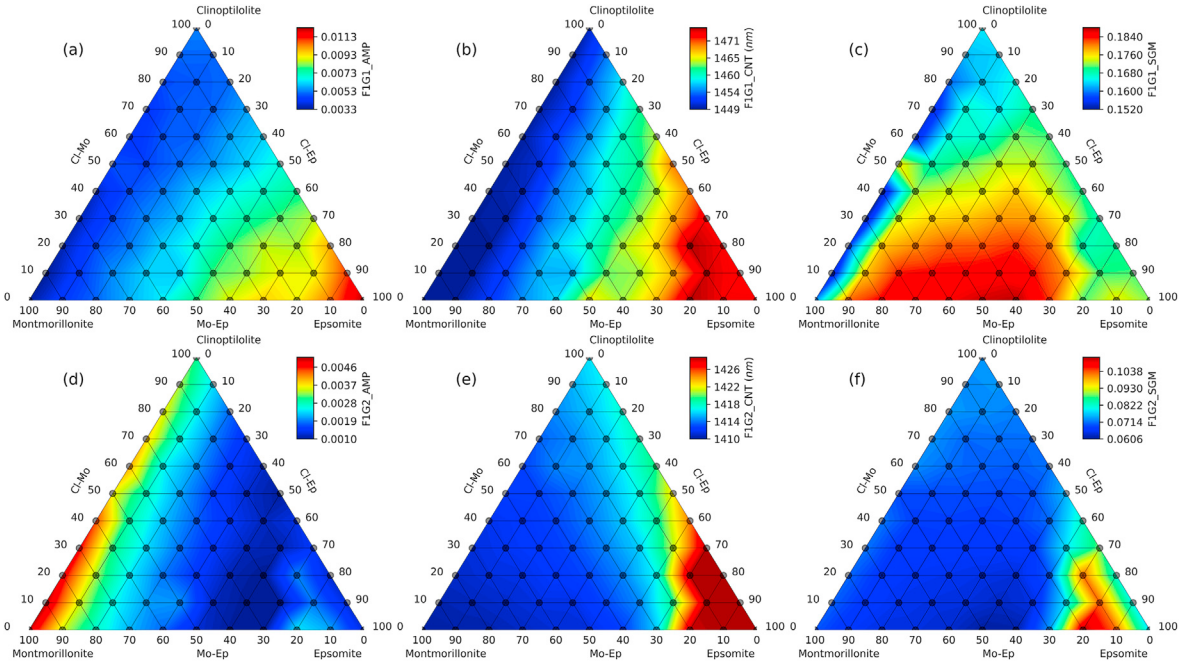


**Fig. 7.** Ternary plots showing the calculated Gaussian curve parameters of feature 1 (F1). a) Amplitude of Gaussian curve 1 of F1 (F1G1-AMP), b) Center wavelength of Gaussian curve 1 of F1 (F1G1-CNT), c) Width of Gaussian curve 1 of F1 (F1G1-SGM), d) Amplitude of Gaussian curve 2 of F1 (F1G2-AMP), e) Center wavelength of Gaussian curve 2 of F1 (F1G2-CNT), f) Width of Gaussian curve 2 of F1 (F1G2-SGM). Linear interpolation was applied between sample points to fill the colors in small triangles in the plots.

a given element  $x$ .

$$\text{ReLU}(x) = \max(x, 0) \quad (9)$$

It retains only positive elements and discards all negative elements by setting the corresponding activations to 0. The Sigmoid function transforms its inputs to outputs in the interval 0 to 1.

$$\text{Sigmoid}(x) = \sigma(x) = \frac{1}{1 + \exp(-x)} \quad (10)$$

Finally, output layer  $O \in \mathbb{R}^{n \times q}$  is calculated as follows,

$$O = H_2 W_3 + b_3 \quad (11)$$

Two common optimization algorithms including Stochastic Gradient Descent (SGD) and Adam (Kingma and Lei, 2015) were used. The term stochastic refers to the fact that each batch of the data is drawn at random. The algorithm computes the outputs and the errors for each batch, then computes the average gradients and adjusts the weights accordingly. This process is repeated for each batch from the training dataset until the loss (mismatch between the prediction and expected target) is minimum (Chollet and Allaire, 2018; LeCun et al., 2015). Adam (name derived from adaptive moment estimation) is also an efficient stochastic optimization algorithm that computes individual adaptive learning rates for different parameters from estimates of first and second moments of the gradients (Kingma and Lei, 2015). The method combines the advantages of two popular optimization algorithms; the ability to deal with sparse gradients in AdaGrad, and the ability to deal with non-stationary objectives in RMSProp (Kingma and Lei, 2015).

The number of training samples is a key factor in ML. Fewer training samples are more likely to overfit the model. With the increase in the amount of training data, the generalization error typically decreases. The generalization error measures how accurately the trained model can predict the outcome for previously unseen data. It is also crucial that the training set used is representative of the cases for which we want to generalize. For this reason, the spectral parameters for another 100 points were derived, interpolating from the nearest three sample points

in the ternary plots. Derived sample points represent the middle point of each small triangle. The interpolations were done only for the eight selected parameters. Spectral parameters for five data points (T89, T120, T131, T134, and T155) were kept aside to test the model. The rest of the samples (160) were randomly divided into two sets, a training dataset containing 66% of the dataset and the rest assigned as a validation dataset. The validation dataset was used to calculate the accuracy (root mean square error; RMSE) of the model after training the DNN using the training dataset. To determine the best DNN model for estimating the most accurate mineral abundances for the given spectral data, 48 models were run changing DNN architecture and its hyperparameters: adding different numbers of hidden layers (2 and 3 layers) and changing the number of units in each hidden layer (6 and 10 units), changing the activation function (Sigmoid and ReLU), and changing the optimization algorithm (SGD and Adam). Each model was tested with four learning rates (0.0001, 0.001, 0.01, 0.1), each with 10,000 epochs. The RMSE errors of the model runs are shown in Table 3. This shows that two hidden layer architecture (with six units in each hidden layer) with ADAM optimization and Sigmoid activation function performed better than the others. From that architecture, the two lowest RMSE were archived under 0.001 and 0.01 learning rates (bold numbers in Table 3). Therefore, these two models were evaluated by the test dataset to find the most generalized model.

$$R_n(\lambda) = R_{T53}(\lambda) + N(\lambda) \quad (12)$$

$$N(\lambda) = \left( \frac{1}{\sqrt{2\pi}\sigma^2} e^{-\frac{(x-\mu)^2}{2\sigma^2}} \right) * \text{percentage} \quad (13)$$

where  $\mu$  is the mean,  $\sigma$  is the standard deviation, and  $x$  is the size (number of data points). The percentages of added noise are 5%, 10%, 25%, 50%, and 75%. Noise added spectra were smoothed using a Savitzky-Golay filter (Savitzky and Golay, 1964) to get more realistic results. The Savitzky-Golay smoothing function fits a low-degree polynomial through the data points within the local spectral window to derive the processed signal values from the polynomial function. The resultant spectra were

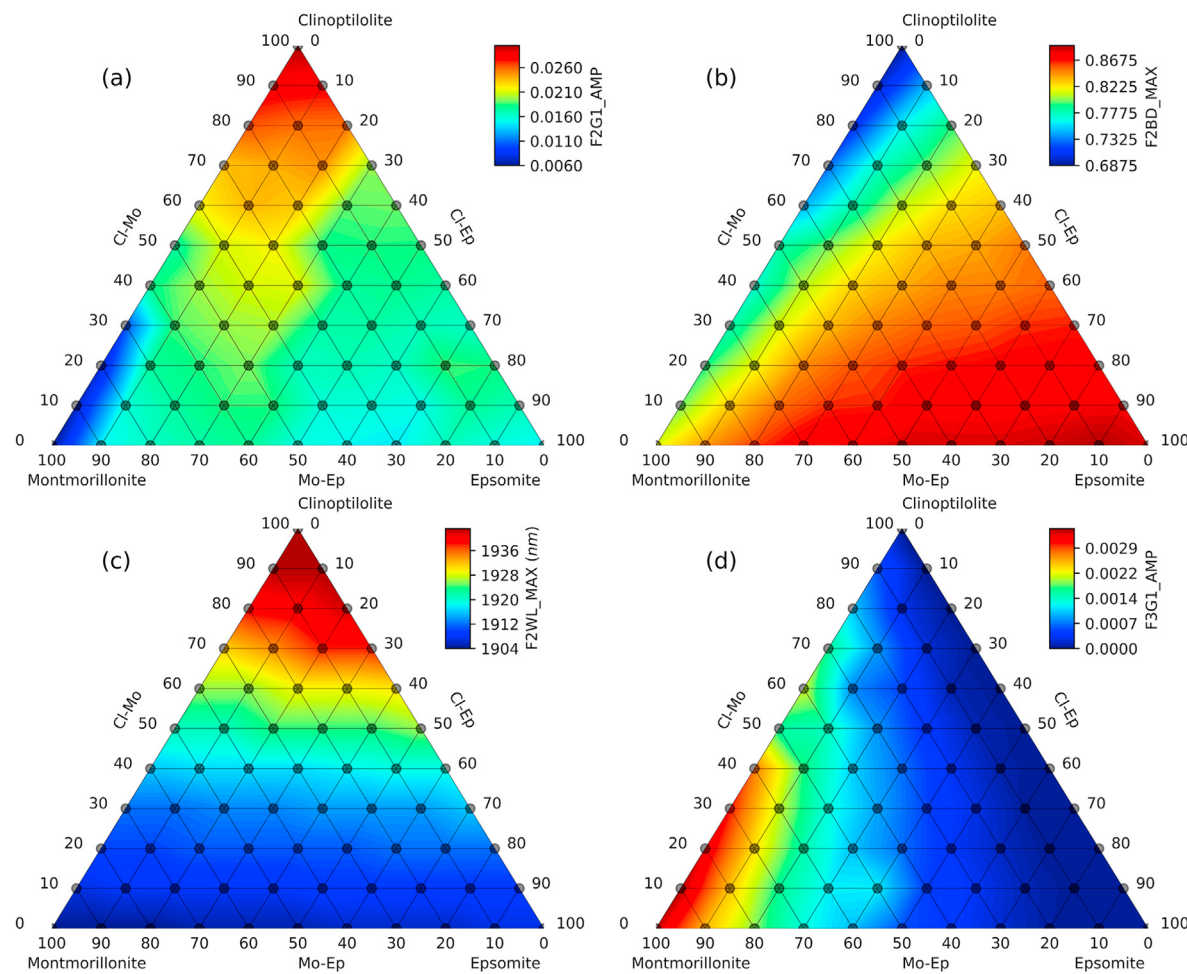


**Fig. 8.** Ternary plots showing the amplitude of Gaussian curve 1 of feature 2 (F2G1-AMP, plot a), maximum band depth of feature 2 (F2BD-MAX, plot b), wavelength at maximum band depth of feature 2 (F2WL-MAX, plot c), and amplitude of Gaussian curve 1 of feature 3 (F3G1-AMP, plot d). Linear interpolation was applied between the sample points to fill the colors in small triangles in the plots.

resampled again into the original laboratory bandpass to derive the Gaussian curve parameters (Fig. 10).

##### 5. Accuracy assessment

From the two selected models, two hidden layer architectures (with 6 hidden units) with ADAM optimization, Sigmoid activation function, and a 0.001 learning rate model gave the best results with the lowest RMSE. The architecture of the winning model is shown in Fig. 9. The accuracy of the predicted results is shown in Fig. 11. This shows that mineral mixtures derived from the interpolated data (T89, T120, T131, T134, and T155) provide more than 90% accuracy based on their predicted mineral abundances. Three out of five montmorillonite and four of five epsomite samples also gave more than 90% of accuracy with the predicted data. However, clinoptilolite samples show less than 50% accuracy and were always predicted as mixture of clinoptilolite and epsomite. One of the epsomite samples was also predicted as a mixture of clinoptilolite and epsomite (with ~10% of montmorillonite). Although the original T53 spectrum was collected from a mineral mixture with 60% clinoptilolite, 20% montmorillonite and 20% epsomite, four out of five noise added T53 spectra predicted that it contained more than 95% clinoptilolite and montmorillonite. The remaining spectrum predicted mainly a mixture of epsomite (>80%) and montmorillonite (<20%) with no clinoptilolite. The 50% noise added spectrum shows an absorption feature at F3, created by the added noise (Fig. 10). The original spectrum shows very low band depth at F3 (Fig. 6c) compared to the noise added spectra

(Fig. 12c). Also, F1 and F2 of the T53 50% noise added spectral features are like the features of the epsomite endmember (Fig. 12). The spectral features of the clinoptilolite (gds125-5841) and montmorillonite (gds149-7646) spectra that deviated the most from their respective endmembers show similar spectral behaviors (Fig. 12a and b). The band strengths of the most deviated predicted compositions are higher than the band strengths of the modeled spectral features (Fig. 12). This could be overcome by normalizing spectral parameters (especially amplitudes and widths of Gaussian curves) using a certain parameter, such as taking the ratio of amplitudes of two different Gaussian curves in the same feature (e.g., F1G1\_AMP/F1G2\_AMP), or normalizing by a Gaussian curve parameter from another feature (e.g., F1G1\_AMP/F2G1\_AMP). Prediction results (values) can be found in Table S2 in the supplementary document.

Even though the overall spectral shape is similar for different samples of the same mineral, grain size variations influence the strength of absorption bands and continuum levels for each sample (Robertson et al., 2016; Swayze et al., 2003). The selected library spectra were taken from different grain sizes, which influence the prediction accuracy. Hunt et al. (1972) observed that the  $1.4 \mu\text{m}$  band depths are strongly influenced by the grain size of the mineral and contaminants. The strength of an absorption is also related to the amount of absorber in the optical path. Clark et al. (1990) noted that the position of the  $\sim 2.2 \mu\text{m}$  absorption band of montmorillonite shifted to a longward position with increasing Ca content. Absorption bands in reflectance spectroscopy are also sensitive to hydration state and cation substitution. The reflectance spectra

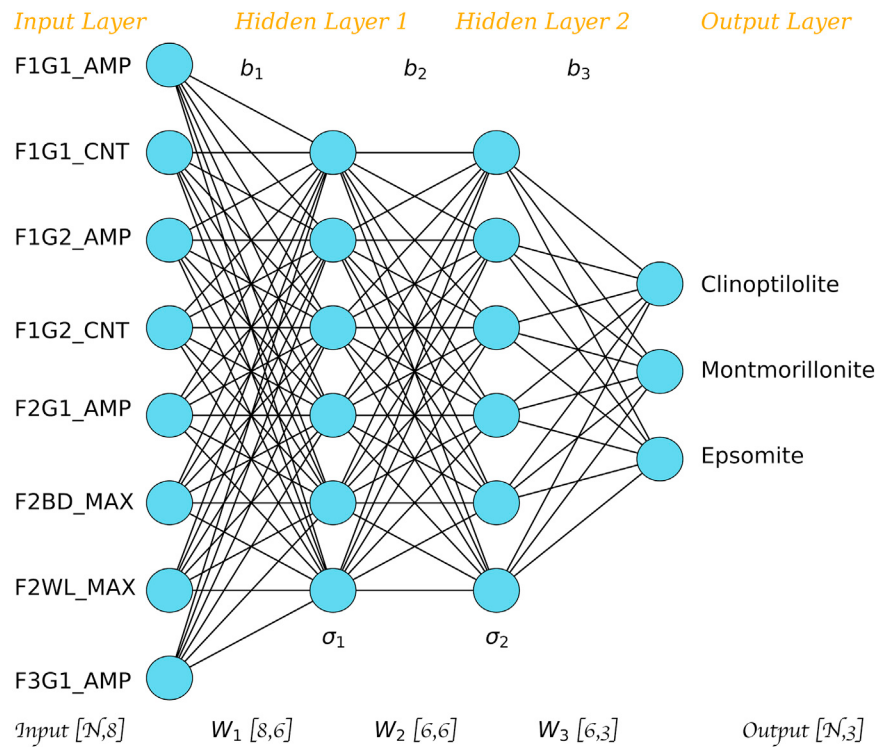


**Fig. 9.** An MLP with eight inputs, two hidden layers containing six hidden units, and three outputs.

**Table 3**

Root Mean Square Error (RMSE) of different models adopted in this study. All models were run for 10,000 epochs.

DNN Architecture	Learning Rate	ADAM with Sigmoid	ADAM with RELU	SGD with Sigmoid	SGD with RELU
<b>8 × 6 × 6 × 3</b>					
	0.0001	0.426	0.684	1.276	0.264
	0.001	<b>0.176</b>	0.434	2.400	2.504
	0.01	<b>0.278</b>	0.367	2.510	2.501
	0.1	2.509	2.496	2.668	2.528
<b>8 × 6 × 6 × 6 × 3</b>					
	0.0001	0.353	0.699	0.214	1.711
	0.001	0.202	0.358	2.230	2.249
	0.01	2.231	0.377	2.213	2.250
	0.1	2.215	2.512	2.437	2.255
<b>8 × 10 × 10 × 3</b>					
	0.0001	0.294	0.380	2.592	0.266
	0.001	0.211	0.245	0.325	2.331
	0.01	0.283	0.288	2.302	2.301
	0.1	2.340	2.350	2.297	2.438

The test dataset consisted of twenty-five samples including spectral parameters derived from the five points that were kept aside before. This was used to assess how well the model identifies mineral mixtures calculated under similar experimental conditions. Fifteen reflectance spectra from available spectral databases were used to assess how well this worked to identify mineral end members from different samples. The library spectra were taken from the RELAB spectral database ([www.planetary.brown.edu/relab](http://www.planetary.brown.edu/relab)), USGS spectral library ([www.usgs.gov/labs/spec-lab](http://www.usgs.gov/labs/spec-lab)), and a spectrum acquired by the authors (Table 4). Library spectra were resampled into laboratory spectra and processed in the same way to derive the spectral parameters. Five noise added spectra simulated the effects of the signal to noise (S/N) ratio on the identification of constituent mineral abundances. The spectrum of sample T53 was resampled to CRISM spectral bandpass and then random noise was added to simulate the spectral quality of these mixtures as seen from orbital data. Five different percentages of random noise with a Gaussian distribution having a zero mean were added to the original spectra.

of variably cation-exchanged SWy montmorillonite show that their

**Table 4**

Library spectra used to test the accuracy of the model.

Spectral ID	Mineral	Specimen Size	Source
T27U	Clinoptilolite + Phillipsite	150 $\mu\text{m}$	personal collection
gds152-5841	Clinoptilolite	–	USGS
gds2-5896	Clinoptilolite	–	USGS
c1ze27	Clinoptilolite	0 - 45 $\mu\text{m}$	RELAB
c1ze28	Clinoptilolite	0 - 45 $\mu\text{m}$	RELAB
gds149-7646	Epsomite ( $\text{MgSO}_4 \cdot 7\text{H}_2\text{O}$ )	–	USGS
c1cc19	$\text{MgSO}_4$ (anhydrous)	0 - 25 $\mu\text{m}$	RELAB
c1cc31	$\text{MgSO}_4$ (hydrous)	0 - 25 $\mu\text{m}$	RELAB
c1jb366	Epsomite $\text{MgSO}_4 \cdot 7\text{H}_2\text{O}$	0 - 45 $\mu\text{m}$	RELAB
c1jb711	Starkeyite $\text{MgSO}_4 \cdot 4\text{H}_2\text{O}$	–	RELAB
c1gr02	Montmorillonite	0 - 100 $\mu\text{m}$	RELAB
c1jb186	Montmorillonite - SWy-2	–	RELAB
c1jb13	Montmorillonite - SWy-1	0 - 125 $\mu\text{m}$	RELAB
c1jb899	Montmorillonite	0-0.2 $\mu\text{m}$	RELAB
cm27-14440	Montmorillonite	–	USGS

absorption band depth at 1.9  $\mu\text{m}$  increases with respect to the absorption band at 2.2  $\mu\text{m}$  from Na-SWy to  $\text{Fe}^{3+}$ -SWy to natural(Na/Ca)-SWy, to Ca-SWy, and to Mg-SWy (Bishop et al., 1994). Cloutis et al. (2002) also observed a general increase in the wavelength position of the 1.4  $\mu\text{m}$  absorption feature from 1.420  $\mu\text{m}$  in K-bearing zeolites, to 1.422  $\mu\text{m}$  in Na-bearing zeolites, and to 1.427  $\mu\text{m}$  in Ca-bearing zeolites. Previous studies show that the position of the 1.9  $\mu\text{m}$  band of montmorillonite shifts to longer wavelength during hydration (e.g., Bishop et al., 1994; Pommerol et al., 2009). Bishop et al. (1994) also noted that Mg and Na montmorillonite measured under a  $\text{H}_2\text{O}$ -purged environment exhibit slightly asymmetric bands centered at 1.91  $\mu\text{m}$ , and under moist conditions, the same samples show a much stronger band at 1.91  $\mu\text{m}$  along with a strong shoulder at 1.97  $\mu\text{m}$ . The shoulder near 1.97  $\mu\text{m}$  is present under moist conditions as it forms due to adsorbed  $\text{H}_2\text{O}$ . Milliken and Mustard (2005) collected spectra from five materials including Na-Ca montmorillonite, Mg-exchanged montmorillonite, clinoptilolite, palagonite, and a reagent-grade  $\text{MgSO}_4 \cdot n\text{H}_2\text{O}$  with initial water contents ranging from 6 to 20 wt% to identify the relationships between the absolute water

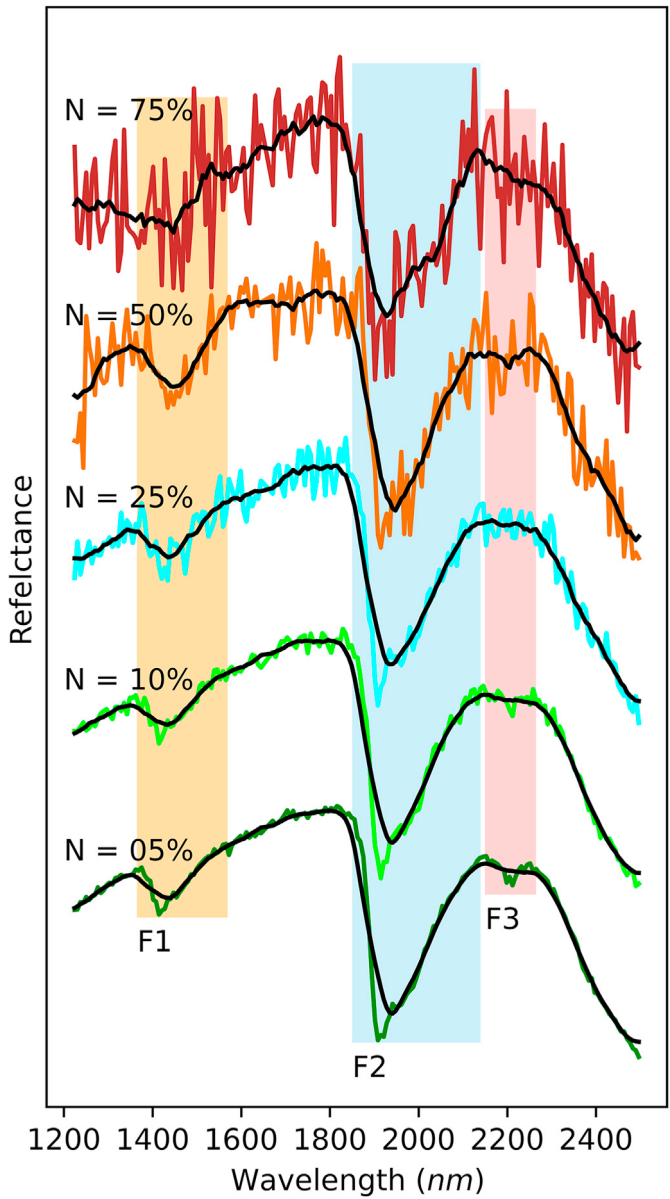


**Fig. 10.** Noise added versions of spectrum T53, resampled to CRISM spectral resolution. Savitzky-Golay Smoothed spectra are shown in black. Percentages of added noise are represented by letter N.

content and water-related absorption bands. There appears to be no correlation between water absorption at  $1.9 \mu\text{m}$  and absolute water content. The  $1.9 \mu\text{m}$  band is also weaker for amorphous material than for well-ordered materials with similar water content. Cloutis et al. (2002) document an increase in the  $1.9 \mu\text{m}$  band position for zeolites from K-bearing zeolites ( $1.911 \mu\text{m}$  average) to Na-bearing zeolites ( $1.913 \mu\text{m}$  average) to Ca-bearing zeolites ( $1.922 \mu\text{m}$  average). Dalton (2003) showed the spectra of different hydration stages of magnesium sulfates ( $\text{MgSO}_4 \cdot n\text{H}_2\text{O}$  for  $n = 0, 1, 1.5, 2, 3, 4, 5, 6$ , and 7) and noted that, with the increase of hydrate stage ( $n$ ), the spectral features near  $1.4$  and  $1.9 \mu\text{m}$  begin to merge and combine creating broad absorption features. Sheppard et al. (2021a,b) measured the changes in near-infrared spectral absorptions of powdered montmorillonite and Mg sulfate mixtures exposed to Mars relevant conditions in a controlled lab setting. They observed that the presence of amorphous Mg sulfate is difficult to identify in physical mixtures that contain more than  $\sim 10\%$  montmorillonite by weight.

Though the shape and position of  $1.4 \mu\text{m}$  and  $1.9 \mu\text{m}$  absorption bands

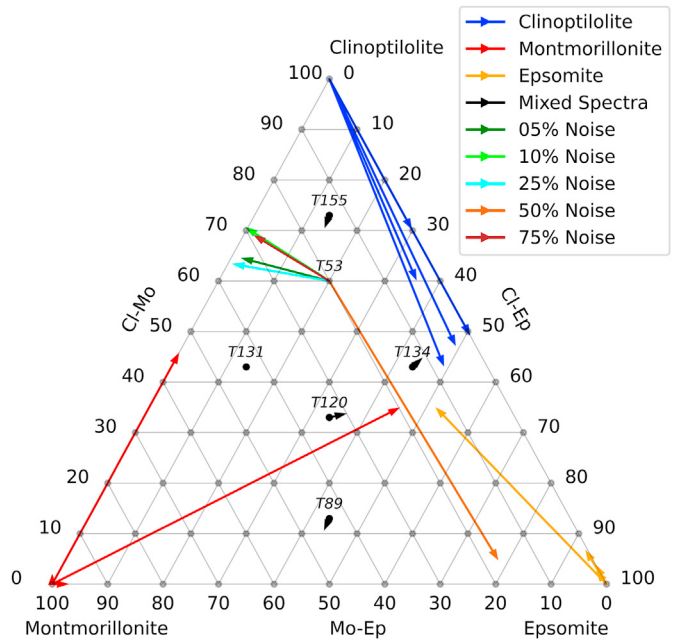


**Fig. 11.** Ternary plot showing the original composition of the mineral/mineral mixture with their predicted compositions. The original composition of minerals represented by 15 library spectra (five spectra from each mineral), spectral parameters derived from mineral mixtures T89, T131, T134, and T155, and five noise added spectra of spectrum T53. Arrowheads show the predicted composition of each mineral mixture. As an example, two out of five montmorillonite spectra identified as a mixture of montmorillonite ( $\sim 55\%$ ) and clinoptilolite ( $\sim 45\%$ ), and mixture of epsomite ( $\sim 45\%$ ), clinoptilolite ( $\sim 35\%$ ), and montmorillonite ( $\sim 20\%$ ). The other three montmorillonite library spectra identified as a montmorillonite with more than 97% accuracy.

in clinoptilolite - montmorillonite mineral mixtures (Fig. 4a) do not change with changes in mineral weight proportion, the  $2.2 \mu\text{m}$  absorption band disappears only in the pure clinoptilolite spectra. Since the absorption band at  $2.2 \mu\text{m}$  is unique for montmorillonite in this mineral assemblage, even though the mineral mixture contains  $\sim 90\%$  of clinoptilolite, it may not be identifiable from the reflectance spectra if it is associated with montmorillonite. The spectra of clinoptilolite - epsomite mineral mixtures shown in Fig. 4 (b) shows the lack of diagnostic absorption feature/s to differentiate these two minerals, except for minute changes in absorption band shape and position of the  $1.4 \mu\text{m}$ ,  $1.9 \mu\text{m}$  bands, which makes them difficult to differentiate using orbital spectral data. This discrepancy is evident in orbital and in-situ observations of Gale crater data. While only Mg-sulfates were visible in the orbital observations, only Ca-sulfates have been seen in in-situ data at certain locations (Sheppard et al., 2021a,b).

Results from previous and current experiments and modeling demonstrate the strong effects of albedo, particle size, water content, and cation substitution for the band parameters (band depth, bandwidth, and band shape) of the  $1.4$ ,  $1.9$  and  $2.2 \mu\text{m}$  absorption bands, in addition to the contribution from constituent mineral abundances. When two opposite correlations are superposed, as seen on real planetary surfaces, this may lead to an even more complex situation, making it more difficult to derive the correct mineral abundances using band parameters. As an example, band strength is positively correlated to surface albedo, though variation in particle size introduces a negative correlation between band strength and surface albedo (Pommerol and Schmitt, 2008). When noise is added into this already complex situation, predicted mineral abundances can be completely incorrect, even using a well-trained DNN. Therefore, it is also important to incorporate the contribution from albedo, particle size, water content, and cation substitution for future models.

This study also demonstrates the application of deep learning

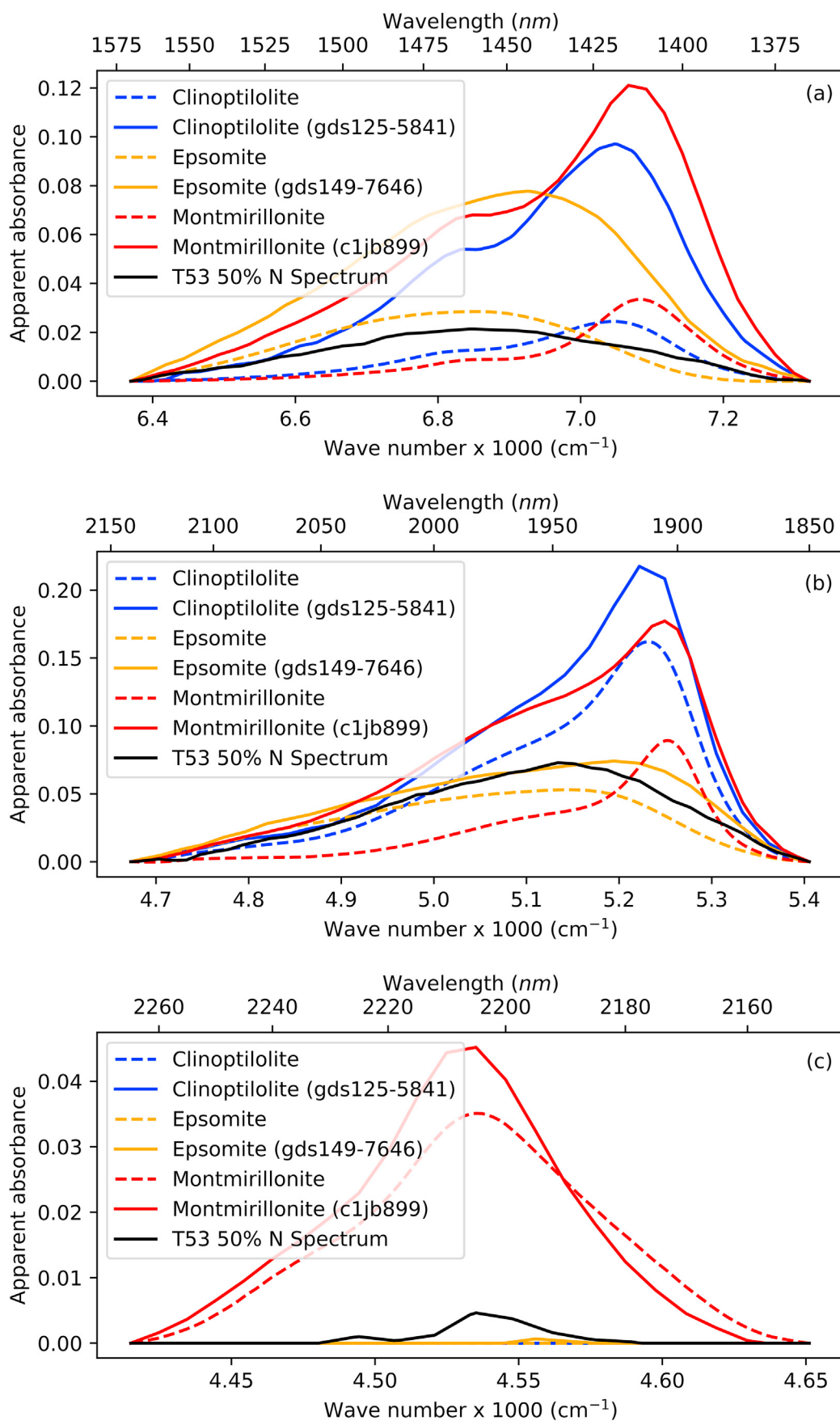


**Fig. 12.** Continuum removed spectra of F1 (plot a), F2 (plot b), and F3 (plot c) of end member spectra (dashed lines) and library spectra, which shows the highest prediction error.

methods which can be implemented onboard future rover missions to identify and predict the mineral abundances using trained DNN models.

## 6. Conclusions

In this study, the efficacy of a combination of spectral deconvolution and deep neural network techniques was examined to estimate mineral abundances of zeolite, Mg-sulfate, and montmorillonite mixtures using their reflectance spectra. Key findings are as follows.

1. The presence of at least ~10% of montmorillonite in a clinoptilolite-montmorillonite mixture can entirely mask the presence of clinoptilolite in SWIR spectral data.
2. If a sample contains higher than ~20% montmorillonite in an epsomite-montmorillonite mixture, the montmorillonite will mask the presence of epsomite in SWIR spectral data.
3. The results show the difficulties of distinguishing clinoptilolite from epsomite even for spectra acquired under laboratory conditions.
4. The absorption bands at  $1.4 \mu\text{m}$ ,  $1.9 \mu\text{m}$ , and  $2.2 \mu\text{m}$  were able to mathematically deconvolve using two normal Gaussian curves, a normal Gaussian curve with a skewed Gaussian curve, and a normal Gaussian curve, respectively.
5. Selecting the correct input features, architecture of DNN, and hyperparameters helps to predict the mineral abundances with higher accuracies.
6. Care must be taken when estimating mineral abundance from a new dataset, even from a well-trained DNN. The new dataset must have similar characteristics to the training dataset to achieve the best results. Normalizing the spectral parameters before feeding it to the DNN might be a good approach, if working with a wide variety of datasets.
7. It is also important to incorporate the contribution from albedo, particle size, water content, and cation substitution for future models.
8. Overall, this study shows the applications and importance of Deep Learning method combined with spectral deconvolution to identify and calculate relative abundances of mineral mixtures using their spectral data. Trained DNN models can be used on board future rover missions for in situ identification of minerals and their relative abundances.

## Credit Author Statement

**Gayantha R. L. Kodikara:** Conceptualization, Methodology, Formal analysis, and Writing – original draft., **Lindsay J. McHenry:** Supervision, Reviewing and Editing, **Freek van der Meer:** Supervision, Reviewing and Editing

## Declaration of competing interest

The authors declare that they have no known competing financial interests or personal relationships that could have appeared to influence the work reported in this paper.

## Acknowledgments

Many thanks to Thomas McCollom at the University of Colorado for acquiring spectral data for field samples, and to USGS and RELAB. Also, thanks to python, PyTorch, and other python modules, and Rstudio developers.

## Appendix A. Supplementary data

Supplementary data related to this article can be found at <https://doi.org/10.1016/j.pss.2022.105579>.

## References

- Bishop, Janice L., Pieters, Carle M., Edwards, John O., 1994. Infrared spectroscopic analysis on the nature of water in montmorillonite. *Clay Clay Miner.* 42 (6), 702–716.
- Brown, Adrian Jon, 2006. Spectral curve fitting for automatic hyperspectral data analysis. *IEEE Trans. Geosci. Rem. Sens.* 44 (No. 6), 1601–1608.
- Cahill, J.T.S., Lucey, P.G., Stockstill-Cahill, K.R., Hawke, B.R., 2010. Radiative transfer modeling of near-infrared reflectance of lunar highland and mare soils. *J. Geophys. Res.* 115, E12013. <https://doi.org/10.1029/2009JE003500>.
- Cahill, J.T.S., Lucey, P.G., Wieczorek, M.A., 2009. Compositional variations of the lunar crust: results from radiative transfer modeling of central peak spectra. *J. Geophys. Res.* 114 (E09001).
- Carter, J., Poulet, F., Bibring, J.-P., Mangold, N., Murchie, S., 2013. Hydrous minerals on Mars as seen by the CRISM and OMEGA imaging spectrometers: updated global view. *J. geoPhy Res. Planets* 118, 831–858.
- Chollet, Francois, Allaire, J.J., 2018. Deep Learning with R. Manning Publications.
- Clark, Roger N., 1981. Water frost and ice: the near-infrared spectral reflectance 0.65 - 2.5 um. *J. Geophys. Res.* 86 (B4), 3087–3096.
- Clark, Roger N., 1995. Reflectance spectra. In: Rock Physics and Phase Relations: A Handbook of Physical Constants. American Geophysical Union, 178–88.
- Clark, Roger N., King, Trude V.V., Klejwa, Matthew, Swayze, Gregg A., 1990. High spectral resolution reflectance spectroscopy of minerals. *J. Geophys. Res.* 95, 680 (No. B8): 12, 653–12.
- Clark, Roger N., Roush, Ted L., 1984. Reflectance spectroscopy: quantitative analysis techniques for remote sensing applications. *J. Geophys. Res.* 89 (No. B7), 6329–6340.
- Cloutis, Edward A., Asher, Pranoti M., Mertzman, Stanley A., 2002. Spectral reflectance properties of zeolites and remote sensing implications. *J. Geophys. Res.* 107 (E9), 5067. <https://doi.org/10.1029/2000JE001467>.
- Cloutis, Edward A., Hawthorne, Frank C., Mertzman, Stanley A., Krenn, Katherine, Craig, Michael A., Marcino, Dionne, Methot, Michelle, et al., 2006. Detection and discrimination of sulfate minerals using reflectance spectroscopy. *Icarus* 184, 121–157.
- Dalton, James Bradley, 2003. Spectral behavior of hydrated sulfate salts: implications for europa mission spectrometer design. *Astrobiology* 3 (4), 771–784.
- Ehlmann, Bethany L., Berger, Gilles, Mangold, Nicolas, Michalski, Joseph R., Catling, David C., Ruff, Steven W., Chassefière, Eric, Niles, Paul B., Chevrier, Vincent, Poulet, Francois, 2013. Geochemical consequences of widespread clay mineral formation in Mars' ancient crust. *Space Sci. Rev.* 174, 329–364.
- Ehlmann, Bethany L., Mustard, John F., Swayze, Gregg A., Clark, Roger N., Bishop, Janice L., Poulet, Francois, Marais, David J. Des, et al., 2009. Identification of hydrated silicate minerals on Mars using MRO-CRISM: geologic context near Nili Fossae and implications for aqueous alteration. *J. Geophys. Res.* 114 (E00D08). <https://doi.org/10.1029/2009JE003339>.
- Geladi, P., MacDougall, D., Martens, H., 1985. Linearization and scatter-correction for near-infrared reflectance spectra of meat. *Appl. Spectrosc.* 39 (3), 491–500.
- Gendrin, Aline, Mangold, Nicolas, Bibring, Jean-Pierre, Langevin, Yves, Gondet, Brigitte, Poulet, Francois, Bonello, Guillaume, et al., 2005. Sulfates in martian layered terrains: the OMEGA/Mars express view. *Science* 307, 1587–1591.
- Hapke, Bruce, 1981. Bidirectional reflectance spectroscopy. *J. Geophys. Res.* 86 (B4), 3039–3054.
- Hapke, Bruce, 1993. Theory of reflectance and emittance spectroscopy. In: Topics in Remote Sensing, vol. 3. Cambridge University Press.
- Hay, Richard L., 1966. Zeolites and zeolitic reactions in sedimentary rocks. *Special GSA Papers* Number 85, 130.
- Hunt, Graham R., 1977. Spectral signatures of particulate minerals in the visible and near infrared. *Geophysics* 42 (No. 3), 501–513.
- Hunt, Graham R., Salisbury, John W., 1970. Visible and near-infrared spectra of minerals and rocks: I. Silicate minerals. *Mod. Geol.* 1, 283–300.
- Hunt, Graham R., Salisbury, John W., Lenhoff, Charles J., 1972. Visible and near-infrared spectra of minerals and rocks: V. Halides, phosphates, arsenates, vanadates and borates. *Mod. Geol.* 3, 121–132.
- Kingma, Diederik P., Jimmy Lei, Ba, 2015. ADAM: a method for stochastic optimization. In: 3rd International Conference on Learning Representations. ICLR 2015, San Diego, CA, USA.
- Kodikara, Gayantha R.L., McHenry, Lindsay J., 2020. Machine learning approaches for classifying lunar soils. *Icarus* 345 (113719).
- Kodikara, Gayantha R.L., Champati ray, P.K., Chauhan, Prakash, Chatterjee, R.S., 2016. Spectral mapping of morphological features on the moon with MGM and SAM. *Int. J. Appl. Earth Obs. Geoinf.* 44, 31–41.
- LeCun, Yann, Bengio, Yoshua, Hinton, Geoffrey, 2015. Deep learning (review). *Nature* 521, 436–444.
- Levenberg, Kenneth, 1944. A method for the solution of certain non-linear problems in least squares. *Q. Appl. Math.* 2, 164–168.
- Liu, Dawei, Lin, Li, Sun, Ying, 2015. An improved radiative transfer model for estimating mineral abundance of immature and mature lunar soils. *Icarus* 253, 40–50.
- Marquardt, Donald W., 1963. An algorithm for least-squares estimation of nonlinear parameters. *SIAM J. Appl. Math.* 11 (2), 431–441.
- Milliken, R.E., Grotzinger, J.P., Thomson, B.J., 2010. Paleoclimate of Mars as captured by the stratigraphic record in Gale crater. *Geophys. Res. Lett.* 37, L04201. <https://doi.org/10.1029/2009GL041870>.
- Milliken, Ralph E., Mustard, John F., 2005. Quantifying absolute water content of minerals using near-infrared reflectance spectroscopy. *J. Geophys. Res.* 110. <https://doi.org/10.1029/2005JE002534>. E12001.
- Murchie, S., Arvidson, R., Bedini, P., Beisser, K., Bibring, J.-P., Bishop, J., Boldt, J., et al., 2007. Compact reconnaissance imaging spectrometer for Mars (CRISM) on Mars

- reconnaissance orbiter (MRO). *J. Geophys. Res.* 112 (E05S03). <https://doi.org/10.1029/2006JE002682>.
- Mustard, John F., Pieters, Carle M., 1989. Photometric phase functions of common geologic minerals and applications to quantitative analysis of mineral mixture reflectance spectra. *J. Geophys. Res.* 94 (B10), 13619–13634.
- Noble, Sarah K., Pieters, Carlé M., Hiroi, Takahiro, Taylor, Lawrence A., 2006. Using the modified Gaussian model to extract quantitative data from lunar soils. *J. Geophys. Res.* 111, E11009. <https://doi.org/10.1029/2006JE002721>.
- Parente, Mario, Makarewicz, Heather D., Bishop, Janice L., 2011. Decomposition of mineral absorption bands using nonlinear least squares curve fitting: application to martian meteorites and CRISM data. *Planet. Space Sci.* 59, 423–442.
- Pommerol, Antoine, Schmitt, Bernard, 2008. Strength of the H<sub>2</sub>O near-infrared absorption bands in hydrated minerals: effects of particle size and correlation with albedo. *J. Geophys. Res.* 113 (E10009), 33.
- Pommerol, Antoine, Schmitt, Bernard, Beck, Pierre, Olivier, Brissaud, 2009. Water sorption on martian regolith analogs: thermodynamics and near-infrared reflectance spectroscopy. *Icarus* 204, 114–136.
- Roach, L.H., Mustard, J.F., Murchie, S.L., Bibring, J.-P., Forget, F., Lewis, K.W., Aharonson, O., Vincendon, M., Bishop, J.L., 2009. Testing evidence of recent hydration state change in sulfates on Mars. *J. Geophys. Res.* 114, E00D02. <https://doi.org/10.1029/2008JE003245>.
- Robertson, K.M., Milliken, R.E., Li, S., 2016. Estimating mineral abundances of clay and gypsum mixtures using radiative transfer models applied to visible-near infrared reflectance spectra. *Icarus* 277, 171–186.
- Rossmann, George R., 1988. Vibrational spectroscopy of hydrous components. In: Hawthorne, F.C. (Ed.), *Spectroscopic Methods in Mineralogy and Geology, Reviews in Mineralogy*. No.18:193–206. Mineralogical Society of America.
- Roush, Ted L., Bishop, Janice L., Brown, Adrian J., Blake, David F., Bristow, Thomas F., 2015. Laboratory reflectance spectra of clay minerals mixed with Mars analog materials: toward enabling quantitative clay abundances from Mars spectra. *Icarus* 258, 454–466.
- Roush, Ted L., Singer, Robert B., 1986. Gaussian analysis of temperature effects on the reflectance spectra of mafic minerals in the 1-um region. *J. Geophys. Res.* 91, B10): 10, 301–10, 308.
- Savitzky, Abraham, Golay, Marcel J.E., 1964. Smoothing and differentiation of data by simplified least squares procedures. *Anal. Chem.* 36 (8), 1627–1639.
- Schmidhuber, Jurgen, 2015. Deep learning in neural networks: an overview. *Neural Network* 61, 85–117.
- Sheppard, Rachel Y., Milliken, Ralph E., Robertson, Kevin M., 2021a. Presence of clay minerals can obscure spectral evidence of Mg sulfates: implications for orbital observations of Mars. In: 52nd Lunar and Planetary Science Conference. LPI Contrib., p. 2548, 1560.pdf.
- Sheppard, Rachel Y., Thorpe, Michael T., Fraeman, Abigail A., Fox, Valerie K., Milliken, Ralph E., 2021b. Merging perspectives on secondary minerals on Mars: a review of ancient water-rock interactions in Gale crater inferred from orbital and in-situ observations. *Minerals* 11 (986).
- Shkuratov, Yu G., Kreslavsky, M.A., Ovcharenko, A.A., Stankevich, D.G., Zubko, E.S., Pieters, C., Arnold, G., 1999. Opposition effect from clementine data and mechanisms of backscatter. *Icarus* 141, 132–155.
- Stack, K.M., Milliken, R.E., 2015. Modeling near-infrared reflectance spectra of clay and sulfate mixtures and implications for Mars. *Icarus* 250, 332–356.
- Sun, Vivian Z., Milliken, Ralph E., 2015. Ancient and recent clay formation on Mars as revealed from a global survey of hydrous minerals in crater central peaks. *J. geoPhy Res. Planets* 120, 2293–2332.
- Sunshine, Jessica M., Pieters, Carle M., 1993. Estimating modal abundances from the spectra of natural and laboratory pyroxene mixtures using the modified Gaussian model. *J. Geophys. Res.* 98 (E5), 9075–9087.
- Sunshine, Jessica M., Pieters, Carle M., Pratt, Stephen F., 1990. Deconvolution of mineral absorption bands: an improved approach. *J. Geophys. Res.* 95 (B5), 6955–6966.
- Swayze, Gregg A., Clark, Roger N., Goetz, Alexander F.H., Chrien, Thomas G., Gorelick, Noel S., 2003. Effects of spectrometer band pass, sampling, and signal-to-noise ratio on spectral identification using the tetracorder algorithm. *J. Geophys. Res.* 108 (E95105).
- Tarantola, Albert, Valette, Bernard, 1982. Generalized nonlinear inverse problems solved using the least squares criterion. *Rev. Geophys. Space Phys.* 20 (No. 2), 219–232.
- Trang, David, Lucey, Paul G., 2019. Improved space weathering maps of the lunar surface through radiative transfer modeling of kaguya multiband imager data. *Icarus* 321, 307–323.
- Vaniman, David T., Bish, David L., Chipera, Steve J., Fialips, Claire I., William Carey, J., Feldman, William C., 2004. Magnesium sulphate salts and the history of water on Mars. *Nature* 431, 663–665.
- Wang, Alian, Jolliff, Bradley L., Liu, Yang, Connor, Kathryn, 2016. Setting constraints on the nature and origin of the two major hydrous sulfates on Mars: monohydrated and polyhydrated sulfates. *J. geoPhy Res. Planets* 121, 678–694.
- Warren, John K., 2016. *Evaporites: A Geological Compendium*. Springer International Publishing.
- Weitz, Catherine M., Noe Dobrea, Eldar, Wray, James J., 2015. Mixtures of clays and sulfates within deposits in western melas chasma, Mars. *Icarus* 251, 291–314.
- Wray, J.J., Milliken, R.E., Dundas, C.M., Swayze, G.A., Andrews-Hanna, J.C., Baldrige, A.M., Chojnacki, M., et al., 2011. Columbus crater and other possible groundwater-fed paleolakes of Terra sirenum, Mars. *J. Geophys. Res.* 116 (E01001), 41.
- Wray, James J., Murchie, Scott L., Squyres, Steven W., Seelos, Frank P., Tornabene, Livio L., 2009. Diverse aqueous environments on ancient Mars revealed in the southern highlands. *Geology* 37 (11), 1043–1046.